First-Principles Simulation of the (Li−Ni−Vacancy)O Phase Diagram and Its Relevance for the Surface Phases in Ni-Rich Li-Ion Cathode Materials

Hena Das,[*,†,‡] Alexander Urban,[†,‡] Wenxuan Huang,[‡,§] and Gerbrand Ceder[*,†,‡,§]

[†]Department of Materials Science and Engineering, University of California, Berkeley, California 94720, United States
[‡]Materials Science Division, Lawrence Berkeley National Laboratory, Berkeley, California 94720, United States
[§]Department of Materials Science and Engineering, MIT, Cambridge, Massachusetts 02139, United States

S *Supporting Information*

ABSTRACT: Despite several reports on the surface phase transformations from a layered to a disordered spinel and a rock-salt structure at the surface of the Ni-rich cathodes, the precise structures and compositions of these surface phases are unknown. The phenomenon, in itself, is complex and involves the participation of several contributing factors. Of these factors, transition metal (TM) ion migration toward the interior of the particle and hence formation of TM-densified surface layers, triggered by oxygen loss, is thermodynamically probable. Here, we simulate the thermodynamic phase equilibria as a function of TM ion content in the cathode material in the context of lithium nickel oxides, using a combined approach of first-principles density functional calculations, the cluster expansion method, and grand canonical Monte Carlo simulations. We developed a unified lattice Hamiltonian that accommodates not only rock-salt like structures but also topologically different spinel-like structures. Also, our model provides a foundation to investigate metastable cation compositions and kinetics of the phase transformations. Our investigations predict the existence of several Ni-rich phases that were, to date, unknown in the scientific literature. Our simulated phase diagrams at finite temperature show a very low solubility range of the prototype spinel phase. We find a partially disordered spinel-like phase with far greater solubility that is expected to show very different Li diffusivity compared to that of the prototype spinel structure.
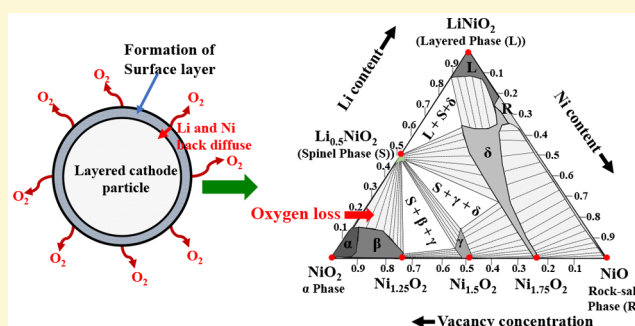
INTRODUCTION

Layered Ni-rich complex oxides are a popular choice as cathode materials for lithium-ion rechargeable batteries because of their high capacity. In particular, layered $LiNi_{0.8}Co_{0.15}Al_{0.05}O_2$ (NCA) and $LiNi_{x'}Mn_{x''}Co_{(1-x'-x'')}O_2$ (NMC) materials offer very high capacity and excellent rate capability.[1] The parent lithium nickel oxide ($LiNiO_2$) itself possesses several drawbacks, such as nonstoichiometry of $Li_{1-x}Ni_{1+x}O_2$[2−4] and low thermal stability.[5−8] In view of these disadvantages of the parent material, attempts to improve the electrochemical properties of Ni-based cathode materials led to doping strategies with other metal ions, such as Co, Al, Mn, Ti, Mg, etc.[9−15] For example, in the NCA compounds, 15% cobalt doping improves the stoichiometry and cation layering of the material and 5% Al ions are believed to lead to improved thermal stability. As most layered cathodes, Ni-rich materials show a rise in impedance when charged to high voltages.[16−20] This phenomenon, reportedly, is triggered by surface phase transformation of these materials from layered to disordered spinel-like and/or rock-salt-like structures, conjectured to occur due to oxygen loss followed by cation densification.[16−20] Through high-resolution transmission electron microscopy (HRTEM)

measurements employing selected area electron diffraction (SAED) and electron loss spectroscopy, the formation of rock-salt surface phases along with disordered spinel subsurfaces has been reported in NCA and NMC materials.[18−23] Although multiple reports describe the irreversible phase transformations that occur at the surface of Ni-rich cathode particles during charge−discharge cycles, the exact cation composition of these surface phases as well as the kinetics of the phase transformations remains unknown. Due to the low mass of the Li ions, it is difficult to experimentally detect Li site occupancy at the particle surface. However, relative arrangements between Li and TM ions have a significant bearing upon Li diffusion and the voltage of the cathode materials.[24,25] Therefore, in order to improve the functionality of these materials, it is imperative to understand the cation configuration of the surface phases.

Oxygen loss at high voltages is a common phenomenon for most Li-ion cathode materials. One of the direct consequences of the oxygen loss at the cathode surface is the loss of oxygen
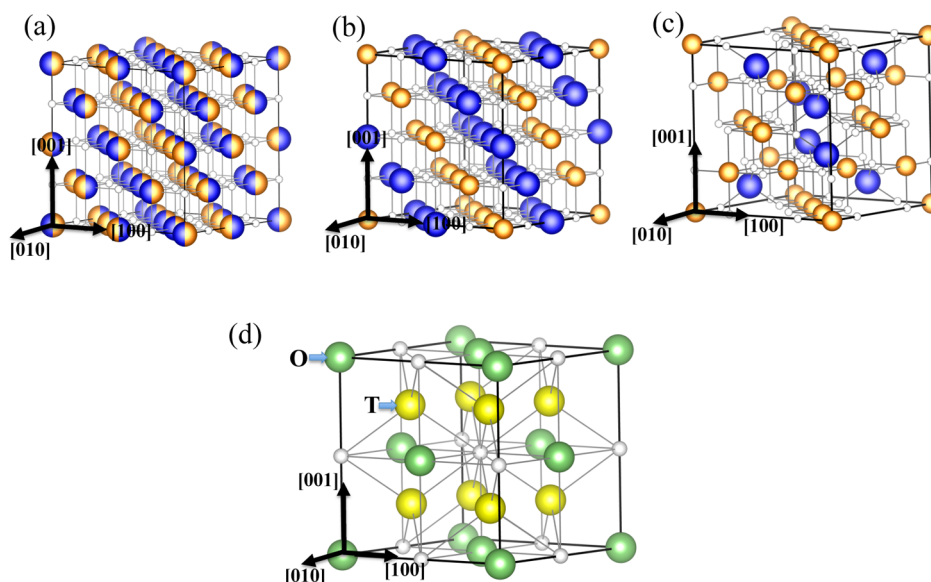
Figure 1. (a−c) Cation arrangement of the rock-salt, layered, and spinel structures, respectively. Blue and orange spheres denote Li and Ni ions, respectively. The white spheres represent O^{-2} ions. (d) Host structure, where octahedral (O) and tetrahedral (T) sites are shown using green and yellow spheres, respectively.

coordination of the cations, which can lead the cations to migrate toward the interior of the cathode particle. Owing to their lower mass and formal charge, Li ions are expected to diffuse faster than transition metal (TM) ions. Therefore, an increase in the TM concentration at the surface within the same oxygen lattice framework is expected, which in turn can lead to the formation of irreversible surface phase transformations. In the present study, in order to understand the cation configuration of the TM-densified surface phases, we simulated thermodynamic phase equilibria as a function of Li, TM, and vacancy occupancy within a fixed oxygen lattice framework. We considered $LiNiO_2$−NiO_2−NiO as a model system. Of all TM ions in NCA and NMC cathode materials, we have singled out Ni in our simulated model since it occurs in the highest concentration. Also, the loss of oxygen leads to the formation of mobile Ni^{+2} ions, as compared to Co^{+3} and Al^{+3} ions, which is expected to lead to Ni migration toward the bulk with greater ease.

The prototype layered, spinel, and rock-salt phases, under discussion in the context of surface phase transitions, share a common close packed fcc oxygen framework, as illustrated in Figure 1. In the rock-salt structure the cations are randomly arranged in the fcc octahedral sites. Whereas the ordered layered structure, $LiNiO_2$, forms alternate layers of Li and Ni planes along the fcc [111] direction (see Figure 1c), the conventional spinel structure, $LiNi_2O_4$, consists of ordered Ni layers along the cubic [100] direction and tetrahedral sites occupied by Li ions (see Figure 1c). To understand the cation configuration in which these phases can exist, we developed a ternary Li−Ni−vacancy lattice model based on the cluster expansion method. In addition to the NiO rock-salt phase, which is the only known Ni excess phase in the literature, our model leads us to predict other Ni excess phases, the existence of which has, so far, neither been experimentally observed nor theoretically predicted. Through grand canonical Monte Carlo (GCMC) simulations based on the ternary model, we discuss the stability range for each phase at finite temperature. We present comparative structural analysis of the predicted Ni-

excess phases with respect to the prototype layered, spinel, and rock-salt structures.

■ METHODS

Construction of a Material-Specific Lattice Model. In this article, we computationally model the ternary phase diagram at finite temperature for the $LiNiO_2$−NiO_2−NiO system through GCMC simulations. GCMC simulations are carried out based on a lattice model constructed using the cluster expansion method[26−28] as implemented in the Clusters Approach to Statistical Mechanics (CASM) software.[29−32] Within the cluster expansion (CE) formalism, the variation of the energy with site occupancy is expanded using a set of cluster functions, Φ_α. In the present study, the ternary cluster functions Φ_α are defined as a product of the nonorthogonal basis set $\{1, \sigma_i, \sigma_i^2\}$, where σ_i denotes cation occupancy of the ith site that is part of cluster α. The configuration energy as a function of occupation variable σ, $E(\sigma)$, for a ternary system is written as

$$E(\sigma) = E_0 + \sum_\alpha m_\alpha J_\alpha \Phi_\alpha \tag{1}$$

where α is a cluster of lattice sites and the summation is over all inequivalent clusters with a multiplicity of m_α. E_0 is the point energy term, and the expansion coefficients, J_α, are called effective cluster interactions (ECIs). It has been observed that in practice the ECIs rapidly approach zero with an increase in the number of lattice sites and distance between atoms in the cluster α. Therefore, one can construct a lattice model using a finite number and size of clusters. The material-specific value of the ECIs is determined by fitting eq 1 to the first-principles calculated energies for a series of representative cation configurations at different lithium nickelate chemical compositions. The cluster expansion approach can be formally justified from a systematic coarse graining of the partition function,[33,34] and its binary version has been used extensively to study configurational order in oxides.[35−37]

As discussed before, the rock-salt, layered, and spinel structures share a common closed packed fcc oxygen lattice as shown in Figure 1a−c, respectively. We therefore consider, within the $Fm\bar{3}m$ oxygen lattice, the interstitial 4a octahedral sites and 8c tetrahedral sites (see Figure 1d), in which the presence of the Li (Ni) cations is associated with an Ising spin $\sigma = 1$ ($\sigma = 0$), whereas a vacancy (☐) is associated with $\sigma = -1$.

The ternary lattice model Hamiltonian was constructed by fitting eq 1 to the energy of 650 ordered arrangements of Li, Ni, and vacancies calculated using the GGA+U method. An optimal set of clusters that minimizes the cross-validation (CV) score was determined using the compressive sensing method.[38] Exact ground state procedures[39] integrated with a maximum satisfiability[40] solver have been applied to identify possible new ground states of the cluster expansion. The predicted ground states were then calculated with the GGA+U method and included in the input data set. The final Hamiltonian, which is constructed with an ∼18 meV/oxygen CV score, consists of 98 clusters with a maximum cluster size of four and maximum distance of 7.0 Å between any two points in the cluster. The cluster expansion error increases with the increase of the energy distance from the convex hull of stability, i.e., the error is smaller for the low-energy structures, as shown in Figure S1.

First-Principles Calculations. All first-principles energy calculations are performed within the density functional theory (DFT) framework[41] using the plane wave pseudopotential method as implemented in the Vienna Ab initio Simulation Package (VASP).[42] The exchange-correlation functionals are approximated by the generalized gradient approximation (GGA) with the PBE form of the exchange correlation functional.[43] We use projector augmented wave (PAW) potentials[44] and a kinetic energy cutoff for expansion of wave functions of 520 eV. The Hellmann−Feynman forces were converged to 0.01 eV/Å. The rotationally invariant scheme by Dudarev et al.[45] was used for the Hubbard U correction to GGA (GGA+U). For Ni 3d states, we chose U_{eff} = 6.0 eV from ref 46, which was estimated from experimental binary formation enthalpies. We cross-checked our calculations by varying the value of the U parameter as well as by employing the HSE screened Coulomb hybrid density functional[47−49] wherever we felt necessary. For all calculations, ferromagnetic spin arrangement between Ni spins was considered.

Construction of the Ternary Phase Diagram. Monte Carlo simulations in the grand canonical ensemble (GCMC) were carried out to determine phase equilibria at a fixed chemical potential and temperature. The grand canonical potential, Ω, is given by

$$\Omega(\mu_{Li}, \mu_{Ni}) = E(x_{Li}, x_{Ni}) - x_{Li}\mu_{Li} - x_{Ni}\mu_{Ni} \qquad (2)$$

where μ_{Li} (μ_{Ni}) is the Li (Ni) chemical potential and x_{Li} (x_{Ni}) is the Li (Ni) content. During each GCMC run, the ensemble-averaged cation concentration (x_{Li}, x_{Ni}) and corresponding grand canonical energy were collected. At a fixed temperature, cation concentration profiles were calculated by varying the Li and Ni chemical potentials from −6.5 to −5.0 eV. To determine the phase boundaries, the grand canonical free energy at temperature T_0, $\Phi(T_0, \mu_{Li}, \mu_{Ni})$, was calculated from a reference free energy $\Phi_0(T_0, \mu_{Li}^0, \mu_{Ni}^0)$ via

$$\Phi(T_0, \mu_{Li}, \mu_{Ni}) = \Phi_0(T_0, \mu_{Li}^0, \mu_{Ni}^0) - \int_{\mu_{Li}^0}^{\mu_{Li}} \langle N(T_0, \mu_{Li}) \rangle \, d\mu_{Li}$$

$$- \int_{\mu_{Ni}^0}^{\mu_{Ni}} \langle N(T_0, \mu_{Ni}) \rangle \, d\mu_{Ni} \qquad (3)$$

■ RESULTS AND DISCUSSION

Ground State Ternary Phase Diagram. *Cluster Expanded Ternary Model.* Figure 2 illustrates the ground state ternary phase diagram for the LiNiO₂−NiO₂−NiO system determined through the combined approach of DFT and the cluster expansion method (DFT+CE). The phase diagram is shown on an equilateral triangle where the three vertices represent 100% Li (LiNiO₂ composition), 100% vacancy □ (NiO₂ composition), and 100% Ni (NiO composition). The formation energy of any $Li_xNi_{1+x'}\square_{1-x-x'}O_2$ composition with respect to the reference compositions is therefore defined as

$$\Delta_f E = E[Li_xNi_{1+x'}\square_{1-x-x'}O_2] - xE[LiNiO_2]$$

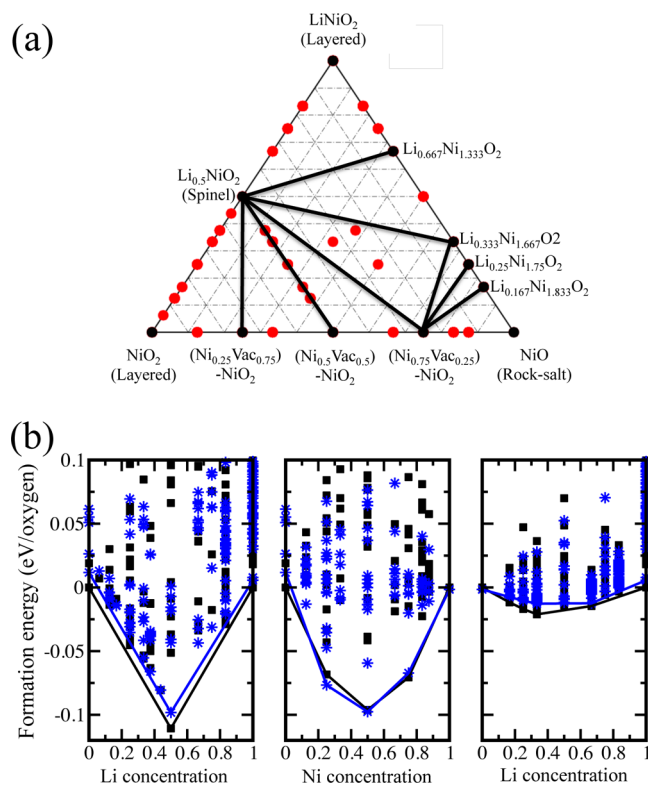$$- 2.0x'E[NiO] - (1 - x - x')E[NiO_2] \qquad (4)$$

(a)

(b)

Figure 2. (a) Ground state Li−Ni−vacancy ternary phase diagram. Black and red solid circles represent stable and metastable phases, respectively. Stable phases are connected via tie lines (black solid lines). (b) Calculated (solid black squares) and cluster expanded (blue stars) formation energies of $Li_xNi_{1+x'}\square_{1-x-x'}O_2$ compositions along the three primary binary lines. Left panel: Li delithiation line from LiNiO₂ to NiO₂; middle panel: oxygen loss line (densification) from NiO₂ to NiO; and right panel: Li, Ni substitution line from NiO to LiNiO₂.

where $E[Li_xNi_{1+x'}\square_{1-x-x'}O_2]$, $E[LiNiO_2]$, $E[NiO]$, and $E[NiO_2]$ denote the corresponding internal energies. The stable single phases are joined through tie lines, i.e., a composition lying on a tie line minimizes its energy by separating into these adjoining stable phases. On the other hand, compositions residing within a tie triangle equilibrate as a three-phase mixture with compositions given by the corners of the triangle. For example, any ternary $Li_xNi_{1+x'}\square_{1-x-x'}O_2$ composition situated inside the LiNi₂O₄−NiO₂−Ni₁.₂₅O₂ tie triangle at 0 K decomposes into the fractions of LiNi₂O₄, NiO₂, and Ni₁.₂₅O₂ stable phases (see Figure 2a). Our DFT+CE model predicts three Ni-excess $Ni_{1+x}\square_{1-x}O_2$ and four Li-deficient $Li_{1-x}Ni_{1+x}O_2$ stable compositions, along with the LiNi₂O₄ spinel phase. The cluster expanded energy hull, as shown in Figure 2b along three binary composition lines, shows good agreement with the GGA+U calculated formation energies. The ECIs are shown in Figure 3a−c. One can divide the full Hamiltonian in three parts. (i) The first part exhibits pair and triplet interactions between tetrahedral (T) sites, as shown in Figure 3a, denoted as H_{TT}. Strong T−T interactions are observed between the third (interplane) and seventh (in-plane) nearest-neighbor (nn) T sites (illustrated in Figure 3d). The strongest negative interaction, approximately −0.15 eV, is of $\sigma^2\sigma^2$ type, which energetically favors 3 nn Li−Li occupancy. Detailed analysis of all T−T interactions shows that Li-occupied tetrahedral shells are energetically favored. (ii) The energy of the configurations in the octahedral (O) sublattice, as
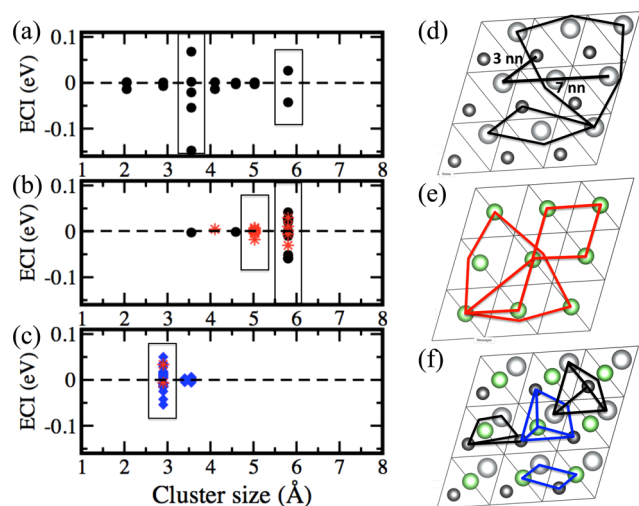
Figure 3. Estimated ECI values for two site (a), three site (b), four site (c) clusters. Black solid circles, red stars, and blue diamonds represent T−T, O−O, and T−O interactions, respectively. Corresponding cluster geometries are illustrated in (d−f). Light gray and dark gray spheres denote tetrahedral sites situated in consecutive alternate layers. Green spheres denote octahedral sites.
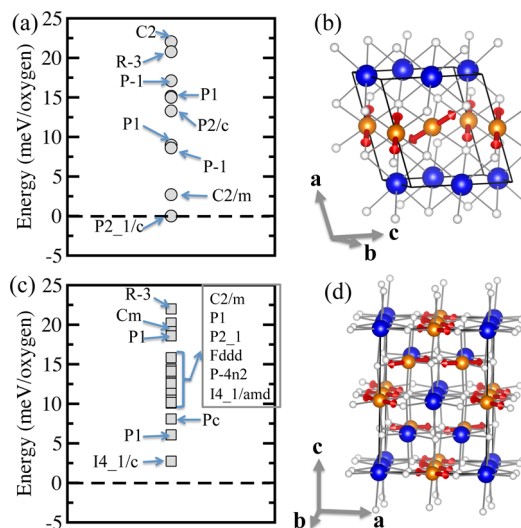

Figure 4. (a, c) Computed energy of distorted layered and spinel-like structures with respect to the ground state layered $P2_1/c$ structure, respectively. Phases within 25 meV/oxygen from the energy hull are shown. (b, d) Illustration of the lowest energy Jahn−Teller (JT) distorted structures for the layered and spinel-like arrangements between Li and Ni, respectively. Associated ordered JT distortions are shown with red arrows, where red arrows denote elongated Ni−O bonds.

shown in Figure 3b,c, is described by triplet and quadruplet interactions within the sub Hamiltonian H_{OO}. The corresponding geometries of these clusters are shown in Figure 3e. (iii) All important interactions between T and O sites included in the sub Hamiltonian H_{TO} are captured within four-site effective cluster interactions (see Figure 3c). The cluster geometries for corresponding strong T−O interactions are illustrated in Figure 3f.

Structure of $Li_{1-x}Ni_{1+x}O_2$ Stable Phases. In the present study, $LiNiO_2$ is a reference composition. In order to find the ground state cation arrangement within this composition, we calculated the energies of 130 Li, Ni cationic arrangements. The undistorted layered structure having lattice symmetry $R\bar{3}m$ is 5 meV/oxygen higher in energy compared to an undistorted spinel-like structure, which is achieved by removing all Li ions from the tetrahedral site in the $LiNi_2O_4$ spinel structure and filling all vacant octahedral sites with Li. This structure is observed in $LiCoO_2$ upon low-temperature synthesis.[50] Ni has +3 valence in $LiNiO_2$, which has the $t_{2g}^6 e_g^1$ ($3d^7$) electronic configuration in the low spin state. With the e_g levels being degenerate, the edge-shared network of NiO_6 octahedra is expected to exhibit strong Jahn−Teller (JT) distortions. Indeed, our computed phonon frequencies at the zone center ($q = 0$) and the zone boundary ($q \neq 0$) symmetry points of the Brillouin zone for both the undistorted $R\bar{3}m$ layered and $Fd\bar{3}m$ spinel-like phases indicate structural instabilities. On the basis of the unstable phonon distortions, 24 and 32 low-symmetry structures were identified for the layered and spinel-like phases, respectively. The relaxed energetics for the distorted layered and distorted spinel-like structures are shown in Figure 4a,c, respectively. We find that the ground state structure has monoclinic $P2_1/c$ symmetry with a layered arrangement of Li and Ni ions (see Figure 4a,b), which is 4 meV/oxygen lower in energy compared to the lowest energy spinel-like phase, the $I4_1/c$ structure (see Figure 4c,d). The details of the optimized crystal structures are given in Table 1. The $P2_1/c$ structure exhibits a zigzag arrangement of JT distortions within the crystallographic bc plane (see Figure 4b). A similar structure

with zigzag JT orbital ordering was discussed and reported earlier.[51−53] The edge-shared NiO_6 octahedra are distorted with two and four Ni−O bonds of length ~2.11 and ~1.91 Å, respectively. These NiO_6 bond statistics are in good agreement with the local structures detected through EXAFS and neutron diffraction studies.[51,54] Although the local JT distortion of our reference phase is in agreement with the experimental reports, a cooperative long-range JT distortion in $LiNiO_2$ has never been observed. JT distortions in $LiNiO_2$ systems so far reported are either random or short ranged.[51,54,55] Here, it is to be noted that the stoichiometric composition is yet to be synthesized. Under experimental synthesis conditions, excess Ni^{+2} ions are always incorporated into the Li layer,[2−4,56−60] creating charge-compensating Ni^{+2} defects in the Ni layer as a result. Ni^{+2} under octahedral oxygen coordination has $t_{2g}^6 e_g^2$ ($3d^8$) electronic configuration, which is not JT active. Therefore, formation of sufficient Ni^{+2} defects may prevent a long-range JT distortion. A long-range JT distortion has been, as a matter of fact, observed in the $C2/m$ structure, in the topologically equivalent $NaNiO_2$ compound.[56,61] This monoclinic structure was also considered along with other arrangements of JT distortions in the present study, but it was found to be higher in energy compared to the $P2_1/c$ structure.

Our DFT+CE model predicts the existence of four stable phases between the layered $LiNiO_2$ and the rock-salt NiO phases (as shown in Figure 2b), none of which, to the best of our knowledge, have been theoretically studied so far. The stable phase at 2/3 Li concentration has monoclinic $C2/c$ symmetry, as illustrated in Figure 5a. The excess 1/3 Ni ions substitute Li within the layered NiO_2. Our spin-polarized GGA +U calculations show inequivalent Ni ions with different oxidation states. A quarter of the Ni ions are situated in the Li layer and have a nominal oxidation state close to +2 (computed magnetic moment ~1.7μ_B), which in turn transforms the oxidation state of a third of the Ni ions in the Ni layer from +3 to +2. The nominal valence state of the remaining Ni is found

Table 1. Optimized Crystallographic Structural Parameters of the LiNiO$_2$ Composition in the Layered and Spinel-Like Phases and the LiNi$_2$O$_4$ Composition in the Prototype Spinel Phase[a]

space group	lattice parameters		atom	site	x	y	z	volume (Å^3/oxygen)
				LiNiO$_2$ (Layered)				
$P2_1/c$	a (Å)	4.98	Li	2a	0.00	0.00	0.00	17.112
	b (Å)	2.93	Ni	2d	0.50	0.00	0.50	
	c (Å)	4.91	O	4e	0.723	0.049	0.247	
	β	107.46						
				LiNiO$_2$ (Spinel-Like)				
$I4_1/c$	a (Å)	5.86	Li	8c	0.0	0.0	0.0	17.085
	c (Å)	7.97	Ni	8d	0.0	0.0	0.5	
			O	16f	0.265	0.776	0.012	
				LiNi$_2$O$_4$ (Spinel)				
$Imma$	a (Å)	5.61	Li	4e	0.00	0.25	0.138	16.453
	b (Å)	5.61	Ni1	4d	0.25	0.25	0.75	
	c (Å)	8.36	Ni2	4b	0.00	0.00	0.50	
			O1	8h	0.00	0.526	0.276	
			O2	8i	0.221	0.25	0.501	

[a]For better comparison, the volume of each phase is normalized with respect to the oxygen content in the system.
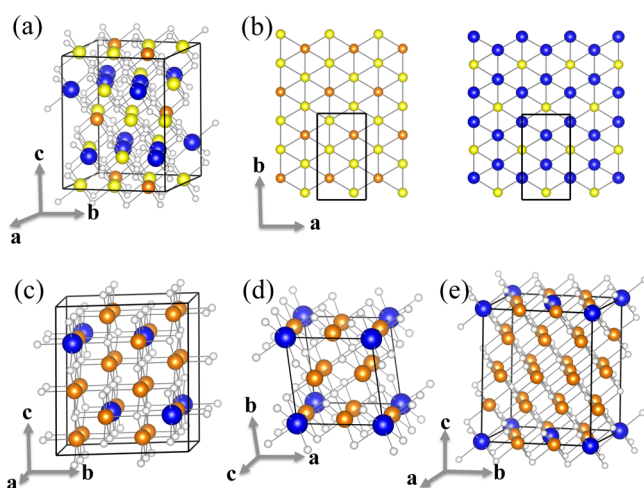

Figure 5. Optimized structures of the Li-deficient phases. (a) Monoclinic $C2/m$ structure of the Li$_{0.667}$Ni$_{1.333}$O$_2$ composition. The blue and white spheres represent Li^{+1} and O^{-2} ions, respectively. The Ni^{+3} and Ni^{+2} ions are denoted by orange and yellow spheres, respectively. (b) Arrangement of Ni^{+2} ions with respect to Ni^{+3} and Li^{+1} ions in two consecutive layers. (c–e) Optimized structures for Li$_{0.333}$Ni$_{1.667}$O$_2$, Li$_{0.25}$Ni$_{1.75}$O$_2$, and Li$_{0.167}$Ni$_{1.833}$O$_2$, respectively. As charge disproportionation of the Ni ions has not been observed in these systems, mixed valent Ni ions are shown with orange spheres.

to be close to +3 (computed magnetic moment ∼1.1μ_B). Although Ni^{+2} ions are surrounded by six nearest-neighbor Li ions in the Li layer, within the Ni layer Ni^{+3} ions are 6-fold coordinated with nearest-neighbor Ni^{+2} ions, as depicted in Figure 5b. The details of the optimized crystal structures are given in Table 2.

At lower Li concentration, three monoclinic phases at $1 - x$ = 1/3, 1/4, and 1/6 Li concentrations are observed. Corresponding crystal structures are shown in Figure 5c–e. The excess Ni ions substitute for Li, except for the composition Li$_{1/3}$Ni$_{5/3}$O$_2$. Within this composition, the concentration of Li ions is the same in both the Li and Ni layers. The details of the optimized crystal structures are given in Table 2.

The observed Ni-rich phases show only weak stability with respect to the end compositions, as indicated by the small energy scale of the energy hull in Figure 2b. This indicates weak

effective interactions between Li and Ni in octahedral sites and is expected to lead to a low order/disorder transition temperature, possibly resulting in the formation of a solid solution between the layered (L) or the rock-salt (R) phase at all but the lowest temperature.

Structure of Ni$_{1+x}$O$_2$ Stable Phases. We now investigate in detail the phases between NiO$_2$ and NiO. The end member NiO$_2$ is the result of fully delithiating the layered LiNiO$_2$ phase (Figure 6a) having an O3 oxygen slab arrangement. Near stoichiometric Ni$_{1+\delta}$O$_2$ can be obtained experimentally through full electrochemical delithiation of a near stoichiometric Li$_{1-\delta}$Ni$_{1+\delta}$O$_2$.[62−64] In our calculations, this phase shows the lowest energy among all Ni−□ configurations sampled in the fcc oxygen framework. This ground state structure has $C2/m$ symmetry contributed by the unstable phonon distortion at the Γ^{+3} symmetry point of the high-symmetry $R\overline{3}m$ structure. A similar structure with higher atomic distortion was reported by Amatucci et al.[63] A different crystal structure with O1 oxygen packing was also reported near the NiO$_2$ composition.[64] In experiments, the presence of more than 7% excess Ni ions, however, stabilizes O3 oxygen packing by destabilizing the O1 structure. With the GGA exchange-correlation functional, the O1 phase was reported to be 7 meV lower in energy than the O3 phase.[65] In order to simplify our model, we did not consider the O1 phase.

The importance of the Ni-excess phases along the NiO$_2$−NiO composition line lies in the fact that they may be formed through two possible ways: (i) due to depletion of oxygen at the surface in the charge−discharge process followed by the back diffusion of Ni ions into the material and (ii) through gradual delithiation of an initial Ni-rich phase.

Between NiO$_2$ and NiO, we found stable phases at x = 1/4, 1/2, and 3/4 excess Ni concentrations. The corresponding optimized crystal structures are shown in Figure 6, and structural details are provided in Table 3. Interestingly, the introduction of excess Ni occurs in a similar manner as that between LiNiO$_2$ and NiO, i.e., excess Ni gradually populates the vacant layer. We did not observe any Ni ions at the tetrahedral site. The phase at x = 1/4 has $R\overline{3}m$ symmetry, with the excess Ni going into the vacant layer (as shown in Figure 6c). The Ni ions in the previously vacant layer are in a +2 valence state with a magnetic moment of ∼1.8μ_B. This extra Ni

Table 2. Optimized Crystallographic Parameters and Atomic Coordinates for the Predicted $Li_{1-x}Ni_{1+x}O_2$ Structures

space group	lattice parameters		atom	site	x	y	z	volume ($Å^3$/oxygen)
					$Li_{0.667}Ni_{1.333}O_2$			
$C2/c$	a (Å)	5.06	Li1	4e	0.0	0.256	0.25	17.696
	b (Å)	8.80	Li2	4e	0.0	−0.087	0.25	
	c (Å)	9.70	Ni1	4c	0.25	0.25	0.0	
	β	100.32	Ni2	4e	0.0	0.585	0.25	
			Ni3	8f	0.249	0.417	0.499	
			O1	8f	0.622	0.075	0.625	
			O2	8f	0.636	0.404	0.616	
			O3	8f	−0.098	0.252	0.886	
					$Li_{0.333}Ni_{1.667}O_2$			
$C2/c$	a (Å)	5.90	Li1	4e	0.0	0.875	0.25	18.147
	b (Å)	8.32	Ni1	8f	0.833	0.125	0.417	
	c (Å)	9.36	Ni2	8f	0.832	0.375	−0.086	
	β	108.51	Ni3	4e	0.0	0.375	0.25	
			O1	8f	0.669	0.376	0.078	
			O2	8f	0.341	0.126	−0.078	
			O3	4e	0.0	0.130	0.25	
			O4	4e	0.0	0.620	0.25	
					$Li_{0.25}Ni_{1.75}O_2$			
$P\bar{1}$	a (Å)	5.11	Li1	1a	0.0	0.0	0.0	18.264
	b (Å)	5.12	Ni1	2i	0.246	0.500	0.877	
	c (Å)	5.92	Ni2	2i	0.499	0.0	0.754	
	α	106.83	Ni3	2i	0.752	0.504	0.628	
	β	90.01	Ni4	1b	0.0	0.0	0.5	
	γ	99.67	O1	2i	0.626	0.753	0.438	
			O2	2i	0.870	0.254	0.320	
			O3	2i	0.613	0.743	−0.064	
			O4	2i	0.872	0.254	0.808	
					$Li_{0.1667}Ni_{1.8333}O_2$			
$C2/m$	a (Å)	5.14	Li1	2a	0.0	0.0	0.0	18.417
	b (Å)	8.89	Ni1	8j	0.752	0.165	0.753	
	c (Å)	9.83	Ni2	4h	0.0	0.833	0.5	
	β	100.09	Ni3	4i	0.751	0.0	0.246	
			Ni4	4g	0.0	0.667	0.0	
			Ni5	2d	0.0	0.5	0.5	
			O1	8j	0.875	0.333	0.624	
			O2	4i	0.125	0.0	0.375	
			O3	8j	0.871	0.171	0.127	
			O4	4i	0.385	0.0	0.127	

insertion into NiO_2 also converts 1/4 of the Ni ions in the Ni layer to the +2 oxidation state. The $Ni^{+2}-\square$ arrangements in the previously vacant layer and $Ni^{+2}-Ni^{+4}$ arrangements in the Ni layer form flower shape patterns, i.e., Ni^{+2} ions are 6-fold coordinated by vacancies ($\square$) and Ni^{+4} ions in the respective layers. Expanded $Ni^{+2}O_6$ (average bond length ∼2.04 Å) chains are connected through contracted $Ni^{+4}O_6$ octahedra (average bond length ∼1.89 Å). This phase will be denoted as β.

The stable structure at $x = 1/2$ has orthorhombic $Cmmm$ symmetry, with columns of Ni^{+2} ions arranged along the crystallographic a axis parallel with columns of vacancies in the previously vacant layer and with Ni^{+4} columns in the Ni layer (see Figure 6d). We will refer to this phase as γ. At this composition, other TM counterparts, such as Co_3O_4 and Fe_3O_4, are known to form spinel structures in which excess TM occupies the tetrahedral sites of the $Fd\bar{3}m$ structure. Using GGA+U with $U = 6.0$ eV applied to the Ni 3d state, the spinel phase is found to be 180 meV/oxygen higher in energy than the γ phase. We investigated the stability of the spinel phase with varying U values from 0 eV (GGA) to 6 eV and with the HSE

functional (the standard value of the mixing parameter (0.25) was used). The results are tabulated in Figure S2. Irrespective of the method employed, the spinel phase was higher in energy compared to the layered γ phase. The results using the HSE functional showed the spinel structure to be unstable by ∼73 meV/oxygen. This value is comparable to the results of GGA +U with $U = 4$ eV and consistent with the fact that no Ni_3O_4 spinel phase is known. The low preference shown by the Ni ions in occupying the tetrahedral site can be understood by the ligand theory discussed in ref 66.

A $Ni_{1.75}O_2$ structure with $Fm\bar{3}m$ symmetry, where 1/4 $\square$ sites are situated at the center of Ni^{+2} hexagons (Figure 6e), is predicted to form. In the Ni layer, the Ni^{+4} ions are also situated at the center of Ni^{+2} hexagons. Note that this structure has the same symmetry as the rock-salt phase but with a doubled unit cell along the cubic [111] direction. This phase will be referred as δ. Detailed crystal structure data is tabulated in Table 3.

Structure of Li_xNiO_2 Stable Phases. At composition $Li_{0.5}NiO_2$, the prototype spinel structure is stabilized (see
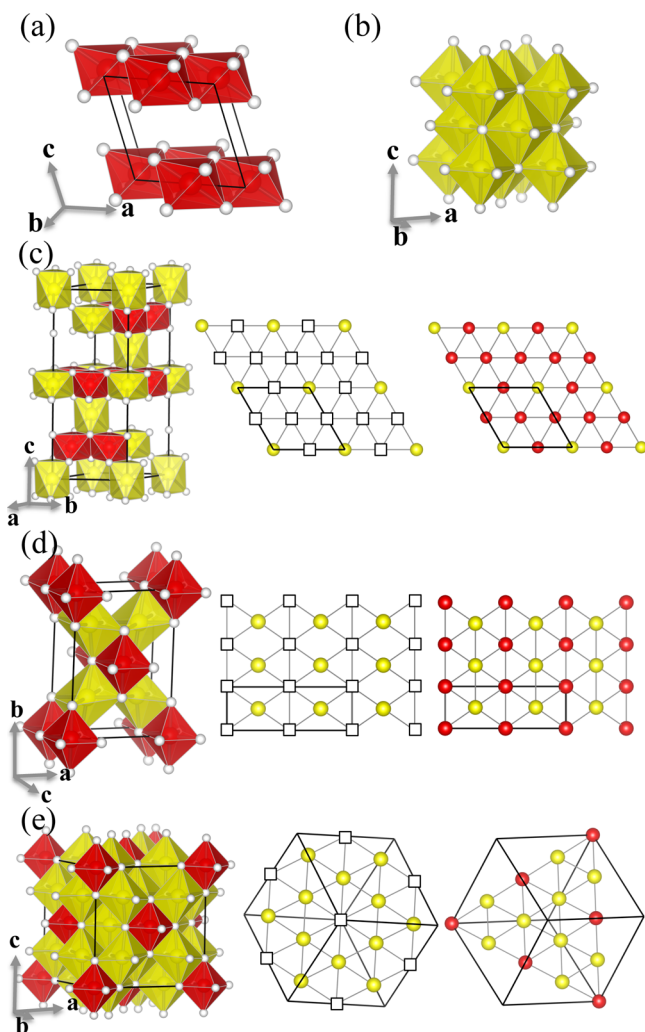
Figure 6. (a, b) Optimized crystal structures of NiO$_2$ and NiO compositions, respectively. The Ni^{+4} and Ni^{+2} ions are denoted with red and yellow spheres, respectively. (c−e) Optimized crystal structures and arrangements between Ni^{+4}, Ni^{+2}, and vacancies (□) are shown for the Ni$_{1.25}$O$_2$, Ni$_{1.50}$O$_2$, and Ni$_{1.75}$O$_2$ compositions, respectively.

Figure 2b). This observation is consistent with previous first-principles studies[67] and with the typical stability of the spinel structure at this composition. The ground state structure contains equal amounts of Ni^{+3} and Ni^{+4}, where regular Ni^{+4}O$_6$ octahedra chains are connected via distorted Ni^{+3}O$_6$ links, resulting in the orthorhombic *Imma* structure. The spinel *Imma* structure was found to be ~60 meV/oxygen lower in energy than the metastable delithiated layered configuration at this concentration. In experiments, as the layered LiNiO$_2$ is partially delithiated, formation of the spinel phase has been observed at elevated temperatures.[5−8] This is in sharp contrast to layered LiMnO$_2$, which transforms to the spinel phase upon Li extraction due to high mobility of the Mn ions.[68−72] Inverse spinel [Ni]$_T$[LiNi]$_O$O$_4$ and pseudo-spinel [LiNi]$_T$[Ni]$_O$O$_4$ configurations, as defined in ref 66, were also considered. We find these phases to be higher in energy compared to the spinel structure.

In practice, delithiation from the near stoichiometric LiNiO$_2$ is known to pass through several ordered layered phases.[73−76] Our ternary cluster expansion can be used to search for the delithiated metastable layered phases by restricting the

occupancy of tetrahedral sites to vacancies. A detailed study of these phases was carried out in ref 65. Results based on this constrained CE are summarized in Figure S3. Our results show seven monoclinic Li−□ ordered structures at $x = 1/3$, 1/5, 3/5, 2/3, 3/4, 5/6, and 7/8 Li concentrations on the layered energy hull. Rhombohedral ordered structures were found at $x = 1/8$, 1/4, and 1/3. Our results agree qualitatively with previous first-principles studies and experimental observations,[73−76] with minor discrepancies.

(Li−Ni−□)O Ternary Phase Diagram at Finite Temperature. Figure 7 shows the equilibrium LiNiO$_2$−NiO$_2$−NiO ternary phase diagram at 300 and 600 K, constructed by employing grand canonical Monte Carlo (GCMC) simulations based on the cluster expanded full lattice Hamiltonian. The corresponding phase diagrams in the Li and Ni chemical potential space are shown in Figures S4 and S5. The shaded regions represent the stability ranges of single phases, and light gray areas are two-phase regions with the dashed tie lines connecting the compositions of both phases in equilibrium. Some single-phase domains touch without a multiphase region between them, representing a second order transition. Three-phase regions are shown by tie triangles (white triangles in Figure 7). The phase diagram constructed at 600 K is similar to the one constructed at 300 K, exhibiting larger regions of solubility in the single phase. Upon cycling cathode materials at room temperature, a sufficient driving force will need to exist to cause transformation into a new phase, and it is likely that compositions can temporarily exist well outside these single-phase domains. Hence, we also plot the 600 K phase diagram to give some idea of how the phase boundaries extend when higher entropy drives extended solubility.

At 300 K, all stable phases observed at 0 K are present, except the Li-deficient Li$_{1−x}$Ni$_{1+x}$O$_2$ phases above $x = 0.5$, as the order−disorder transition temperature of these phases is below 300 K. Additionally, a dilithiated layered phase occurs around Li$_{0.125}$NiO$_2$ stoichiometric composition, which is denoted as α'. The energy of the structure is 14 meV/oxygen above the ground state energy hull, i.e., metastable at 0 K. The corresponding Li-vacancy arrangement in the Li plane is depicted in Figure S3. This phase does not form at 600 K. A phase transition from the ordered λ to the disordered rock-salt phase occurs around 480 K. At 600 K, therefore, the rock-salt phase shares a second order phase boundary with the L phase. As shown in Figure 7a,b, the spinel (S) phase shows a very small solubility range at both 300 and 600 K. This is mostly due to the high energy associated with placing Ni/vacancy in a tetrahedral site, which would be required for the LiNi$_2$O$_4$ composition to move into the Ni-densified part of the phase diagram. This is also consistent with the fact that formation of Ni at the tetrahedral sites has not been reported through experiments for Ni-containing materials such as NCA and NCM. The spinel phase rather coexists with other stable phases that appear in the phase diagram. Upon the addition of Ni along the NiO$_2$−NiO axis, α-NiO$_2$ first transforms to the β phase through a first order transition at 300 K and a second order transition at 600 K, followed by first order transitions from $\beta \rightarrow \gamma \rightarrow \delta \rightarrow$ rock-salt (R) at both temperatures. Among these Ni-excess phases, the δ and R phases exist for a large (Li, Ni, □) composition space. The layered phase also exhibits a significant solubility range at 600 K, which probably leads to the nonstoichiometry of the lithium nickelate compositions.[2−4,56−60]

Table 3. Optimized Crystallographic Parameters and Atomic Coordinates for the Predicted $Ni_{1+x}O_2$ Structures

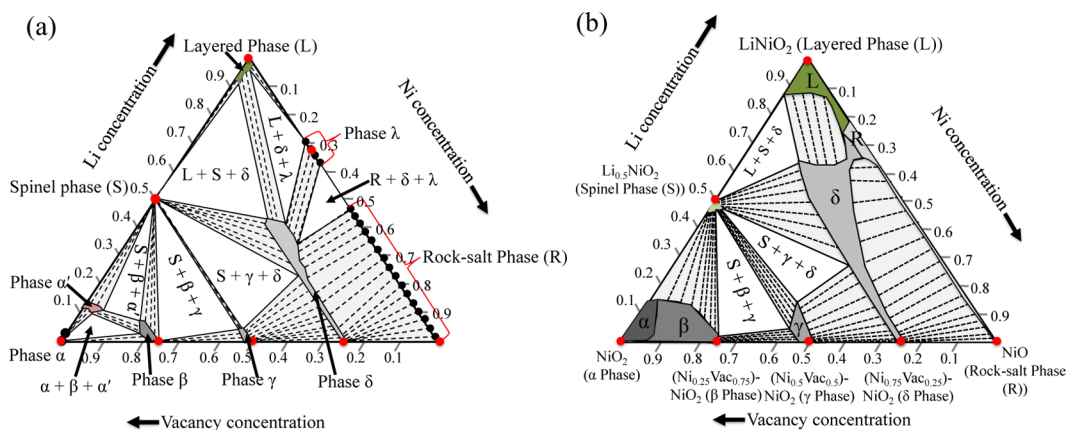| space group	lattice parameters		atom	site	x	y	z	volume (Å³/oxygen)
			NiO_2					
$C2/m$	a (Å)	4.82	Ni	2d	0.00	0.5	0.5	16.390
	b (Å)	2.78	O	4i	0.770	0.00	0.306	
	c (Å)	5.13						
	β	107.78						
			$Ni_{1.25}O_2$					
$R\bar{3}m$	a (Å)	5.67	Ni1	9d	0.5	0.0	0.5	17.021
	c (Å)	14.64	Ni2	3a	0.0	0.0	0.0	
			Ni3	3b	0.0	0.0	0.5	
			O1	18h	0.153	0.847	0.098	
			O2	6c	0.0	0.0	0.769	
			$Ni_{1.50}O$					
$Cmmm$	a (Å)	5.98	Ni1	2c	0.5	0.0	0.5	17.696
	b (Å)	8.25	Ni2	4e	0.25	0.25	0.0	
	c (Å)	2.87	O1	4g	0.295	0.0	0.0	
			O2	4j	0.0	0.273	0.5	
			$Ni_{1.75}O_2$					
$Fm\bar{3}m$	a (Å)	8.35	Ni1	24d	0.0	0.25	0.25	18.223
			Ni2	4a	0.0	0.0	0.0	
			O1	24e	0.774	0.0	0.0	
			O2	8c	0.25	0.25	0.25	
			NiO					
$Fm\bar{3}m$	a (Å)	4.21	Ni	4a	0.0	0.0	0.0	18.685
			O	4b	0.5	0.5	0.5	

Figure 7. (a, b) (Li−Ni−vacancy)O phase diagram calculated at 300 and 600 K, respectively. Shaded and white regions indicate single- and three-phase states, respectively. Two-phase states are shown with dotted lines. Stoichiometric compositions associated with the stable phases are indicated with red spheres.

Figure 8a shows simulated X-ray powder diffraction (XRD) patterns for each single phase considering stoichiometric compositions. We simulated basic XRD patterns using the Monte Carlo output structures at 600 K, as the main motivation of the present study was to understand the cation configuration of these phases. Note that in the Monte Carlo simulations of the CE all lattice parameters are renormalized and no structural distortions are expressed in the Hamiltonian (even though their effect on the energy is included). We therefore ignored the peak shifting or splitting resulting from structural distortions, a qualitative understanding of which can be obtained from the DFT optimized structures. Important peaks are indexed for each single phase according to the associated crystal symmetry. The signature peak that represents the layered ordering between Li and Ni ions along the fcc cubic [111] direction appears around ∼18°. As shown in Figure 8a,

the relative intensity of this peak gets significantly modified with the increase of the Ni content in the system and completely disappears in the rock-salt phase, as expected due the loss of cation ordering with the increase in the Ni concentration. Along with many similarities, these phases exhibit distinct features in the XRD patterns by means of which they may be individually identifiable.

In contrast to powder XRD patterns, symmetry-equivalent reflections are measured individually either through Fourier transformation (FFT) of the HRTEM images or via selective area electron diffraction (SAED) measurements. These methods have been employed largely to identify the phases that appear at the surface of charged NCA and NMC particles.[16−20] As the formation of disordered spinel and rock-salt type surface phases has been repeatedly experimentally reported for the NCA material, comparative characterizations
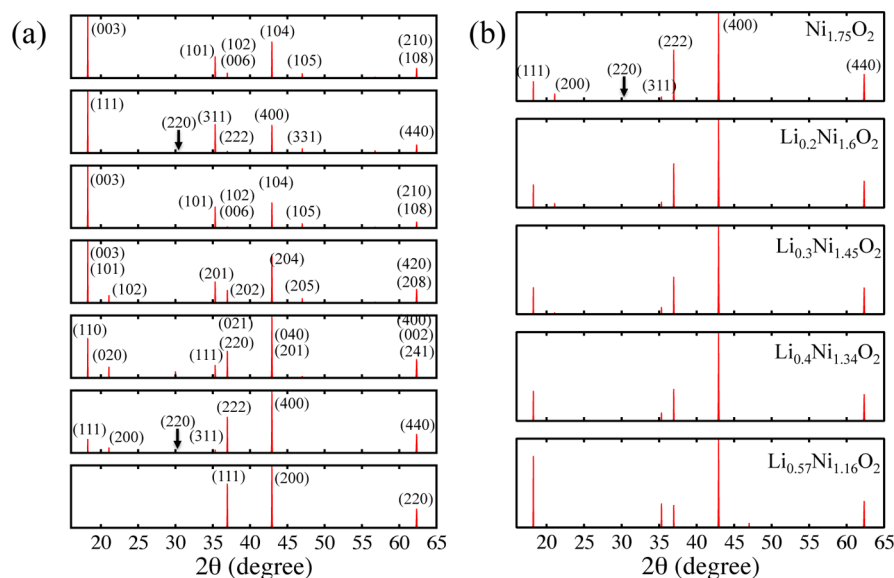
Figure 8. (a) Simulated X-ray powder diffraction patterns for the layered $LiNiO_2$ ($R\bar{3}m$), spinel $LiNi_2O_4$ ($Fd\bar{3}m$), layered NiO_2 ($R\bar{3}m$), β-$Ni_{1.25}O_2$ ($R\bar{3}m$), γ-$Ni_{1.50}O_2$ ($Cmmm$), δ-$Ni_{1.75}O_2$ ($Fm\bar{3}m$), rock-salt NiO ($Fm\bar{3}m$) structures (from the upper most panel to the lower most panel). (b) Simulated X-ray powder diffraction patterns for five compositions of the δ phase.

of the proposed Ni-excess structures with the prototype spinel and rock-salt phases are essential. We observed, among all predicted Ni-excess phases, that the δ structures exhibit remarkable similarities with the cubic spinel phase. The δ phase has cubic $Fm\bar{3}m$ symmetry with a doubled unit cell compared to the rock-salt phase, which leads to the formation of a (111) diffraction peak around $2\theta \sim 18°$, similar to that of the $Fd\bar{3}m$ spinel structure. This peak has 8-fold multiplicity. The spinel and the δ phases show significant diffraction peaks with the same cubic Miller indices and multiplicity. In the stoichiometric composition of the δ phase, the intensity of the (111) peak is much weaker compared to the (400) diffraction (see Figure 8a). However, as shown in Figure 8b, with an increase in the Li content the relative intensity of the (111) peak increases, which implies an increase in the cation ordering. Formation of the spinel phase has been associated with the presence of a weak diffraction peak at (220), which is absent in the layered and rock-salt structures. The intensity of this peak strongly depends on the presence of TM ions at the tetrahedral site. Interestingly, a weak (220) peak is also present in the δ phase. The δ phase exhibits a weak reflection at (200), which is absent in the spinel phase. The intensity of this peak, however, decreases with the increase in the Li concentration in the system (see Figure 8). Therefore, with increasing Li content, the δ phase is expected to look more like the spinel phase.

In this study, we present $LiNiO_2$–NiO_2–NiO ternary phase diagrams computed using first-principles-based techniques. Our results provide several important insights for the study of Ni-rich lithium–metal oxides. As in many lithium–metal oxides, the spinel dominates the phase diagram near the $LiNi_2O_4$ stoichiometry. The strong stability of this phase limits the solubility domain of other phases. In cases where this phase is not present, and metastable partially delithiated layered phases persist instead, the solubility limits of the other phases will be higher, as the equilibrium chemical potentials in a metastable equilibrium are always higher than in a stable equilibrium. This is usually the case during room temperature electrochemical cycling of $LiNiO_2$. Our results also provide important cautions and insights into the processes that occur near the surface of

the cathode where the loss of oxygen upon charging creates extra Ni ions, which then back diffuse into the cathode, creating a "densified zone". This densification region is believed to be responsible for the impedance buildup observed during cycling. Although phase identification in these 10−50 nm densified areas is difficult, one often refers generically to the presence of rock-salt-like and spinel phases. The stoichiometric $LiNi_2O_4$ spinel structure is known to facilitate Li diffusion[24] and therefore is not expected to contribute to the observed rise in ionic impedance in Ni-rich cathode materials. Our phase diagram offers at least an alternative explanation for the observed impedance rise. The novel phases discovered in the Ni-densified region of the phase diagram present a significantly more complex picture than the typically assumed NiO_2−NiO equilibrium. These phases all have a very negative formation energy as compared with the NiO_2−NiO tie line, well outside of the range of typical DFT errors, which gives us high confidence in their prediction. Of these Ni-excess phases, the partially disordered δ phase in particular, which exists for high Li concentration, is very interesting as it shows striking similarities with the prototype spinel structure in its XRD pattern. This δ phase is formed via Li, Ni, and vacancy ordering in the octahedral sites. Despite the structural similarities between the δ and spinel phases, the process of Li-ion diffusion is expected to be much poorer in δ than in spinel, as it does not form a percolating low-energy pathway for Li migration. The similarity of this phase to spinel points to the need for more rigorous characterization of the surface densification products in Ni-rich cathodes in order to understand impedance growth better.

Finally, although our study has been limited to pure Ni systems, it provides implications for other layered oxides and more complex mixed transition metal layered oxides, such as the NCA and NMC cathodes. The driving force to form ordered phases along the NiO_2−NiO axis is due to the large effective ordering interaction between Ni and vacancies. As this interaction is mostly electrostatic in nature, one can expect it to be fairly chemistry agnostic and also to be present in other Li−M−O systems or in mixed metal NCA and NMC cathodes.

Hence, a more complex densification landscape is also likely to be found in these cathodes.

CONCLUSIONS

We have investigated the phase equilibria of Ni-densified phases through first-principles simulated model (Li−Ni−□)O phase diagrams and discussed in detail their relevance for the surface phases reported in Ni-rich Li-ion cathode materials. We observed significant similarities in XRD patterns between the prototype spinel and the proposed δ phase. Hence, we speculate that it is possible that what is claimed to be the observation of a disordered spinel phase at the surface of charged cathodes may actually also be the δ phase. Li transport in the δ phase is expected to be much poorer compared to that in the spinel phase. The structures that we have proposed in our study will introduce vital inputs in the process of characterization of the surface phases observed in Ni-rich cathode materials.

ASSOCIATED CONTENT

Ⓢ Supporting Information

The Supporting Information is available free of charge on the ACS Publications website at DOI: 10.1021/acs.chemmater.7b02546.

Estimated cluster expansion error as a function of the energy distance from the convex hull of stability, computed energetic of the layered and spinel structures of Ni_3O_4 composition, calculated energy hull of layered Li_xNiO_2 compositions, constructed phase diagrams of the (Li−Ni−vacancy)O system in the Li and Ni chemical potential space (PDF)

AUTHOR INFORMATION

Corresponding Authors

*E-mail: hdas@berkeley.edu (H.D.).
*E-mail: gceder@berkeley.edu (G.C.).

ORCID Ⓞ

Hena Das: 0000-0001-5378-066X

Notes

The authors declare no competing financial interest.

ACKNOWLEDGMENTS

REFERENCES

(1) Whittingham, M. S. Lithium Batteries and Cathode Materials. *Chem. Rev.* **2004**, *104*, 4271−4302.

(2) Rougier, A.; Gravereau, P.; Delmas, C. Optimization of the Composition of the $Li_{1−z}Ni_{1+z}O_2$ Electrode Materials: Structural, Magnetic, and Electrochemical Studies. *J. Electrochem. Soc.* **1996**, *143*, 1168−1175.

(3) Peres, J.; Delmas, C.; Rougier, A.; Broussely, M.; Perton, F.; Biensan, P.; Willmann, P. The Relationship Between the Composition of Lithium Nickel Oxide and the Loss of Reversibility During the First Cycle. *J. Phys. Chem. Solids* **1996**, *57*, 1057−1060.

(4) Delmas, C.; Pérès, J.; Rougier, A.; Demourgues, A.; Weill, F.; Chadwick, A.; Broussely, M.; Perton, F.; Biensan, P.; Willmann, P. On the Behavior of the Li_xNiO_2 System: An Electrochemical and Structural Overview. *J. Power Sources* **1997**, *68*, 120−125.

(5) Dahn, J.; Fuller, E.; Obrovac, M.; von Sacken, U. Thermal Stability of Li_xCoO_2, Li_xNiO_2 and λ-MnO_2 and Consequences for the Safety of Li-ion Cells. *Solid State Ionics* **1994**, *69*, 265−270.

(6) Ohzuku, T.; Ueda, A.; Kouguchi, M. Synthesis and Characterization of $LiAl_{1/4}Ni_{3/4}O_2$ (R$\overline{3}$m) for Lithium-Ion (Shuttlecock) Batteries. *J. Electrochem. Soc.* **1995**, *142*, 4033−4039.

(7) Arai, H.; Sakurai, Y. Characteristics of Li_xNiO_2 Obtained by Chemical Delithiation. *J. Power Sources* **1999**, *81-82*, 401−405.

(8) Albrecht, S.; Kümpers, J.; Kruft, M.; Malcus, S.; Vogler, C.; Wahl, M.; Wohlfahrt-Mehrens, M. Electrochemical and Thermal Behavior of Aluminum- and Magnesium-Doped Spherical Lithium Nickel Cobalt Mixed Oxides $Li_{1−x}(Ni_{1−y−z}Co_yM_z)O_2$ (M = Al, Mg). *J. Power Sources* **2003**, *119−121*, 178−183.

(9) Ohzuku, T.; Ueda, A.; Nagayama, M. Electrochemistry and Structural Chemistry of $LiNiO_2$ (R $\overline{3}$m) for 4 V Secondary Lithium Cells. *J. Electrochem. Soc.* **1993**, *140*, 1862−1870.

(10) Delmas, C.; Saadoune, I.; Rougier, A. The Cycling Properties of the $Li_xNi_{1−y}Co_yO_2$ Electrode. *J. Power Sources* **1993**, *44*, 595−602.

(11) Delmas, C.; Saadoune, I. Electrochemical and Physical Properties of the $Li_xNi_{1−y}Co_yO_2$ Phases. *Solid State Ionics* **1992**, *53-56*, 370−375.

(12) Cho, J.; Jung, H.; Park, Y.; Kim, G.; Lim, H. S. Electrochemical Properties and Thermal Stability of $Li_aNi_{1−x}CO_xO_2$ Cathode Materials. *J. Electrochem. Soc.* **2000**, *147*, 15−20.

(13) Gao, Y.; Yakovleva, M. V.; Ebner, W. B. Novel $LiNi_{1−x}Ti_{x/2}Mg_{x/2}O_2$ Compounds as Cathode Materials for Safer Lithium-Ion Batteries. *Electrochem. Solid-State Lett.* **1999**, *1*, 117−119.

(14) Delmas, C.; Ménétrier, M.; Croguennec, L.; Saadoune, I.; Rougier, A.; Pouillerie, C.; Prado, G.; Grüne, M.; Fournès, L. An Overview of the Li(Ni,M)O₂ Systems: Syntheses, Structures and Properties. *Electrochim. Acta* **1999**, *45*, 243−253.

(15) Wang, G.; Zhong, S.; Bradhurst, D.; Dou, S.; Liu, H. $LiAl_\delta Ni_{1−\delta}O_2$ Solid Solutions as Cathodic Materials for Rechargeable Lithium Batteries. *Solid State Ionics* **1999**, *116*, 271−277.

(16) Abraham, D. P.; Twesten, R. D.; Balasubramanian, M.; Kropf, J.; Fischer, D.; McBreen, J.; Petrov, I.; Amine, K. Microscopy and Spectroscopy of Lithium Nickel Oxide-Based Particles Used in High Power Lithium-Ion Cells. *J. Electrochem. Soc.* **2003**, *150*, A1450−A1456.

(17) Zhang, Y.; Wang, C.-Y. Cycle-Life Characterization of Automotive Lithium-Ion Batteries with $LiNiO_2$ Cathode. *J. Electrochem. Soc.* **2009**, *156*, A527−A535.

(18) Wu, L.; Nam, K.-W.; Wang, X.; Zhou, Y.; Zheng, J.-C.; Yang, X.-Q.; Zhu, Y. Structural Origin of Overcharge-Induced Thermal Instability of Ni-Containing Layered-Cathodes for High-Energy-Density Lithium Batteries. *Chem. Mater.* **2011**, *23*, 3953−3960.

(19) Hwang, S.; Chang, W.; Kim, S. M.; Su, D.; Kim, D. H.; Lee, J. Y.; Chung, K. Y.; Stach, E. A. Investigation of Changes in the Surface Structure of $Li_xNi_{0.8}Co_{0.15}Al_{0.05}O_2$ Cathode Materials Induced by the Initial Charge. *Chem. Mater.* **2014**, *26*, 1084−1092.

(20) Sallis, S.; Pereira, N.; Mukherjee, P.; Quackenbush, N. F.; Faenza, N.; Schlueter, C.; Lee, T.-L.; Yang, W. L.; Cosandey, F.; Amatucci, G. G.; Piper, L. F. J. Surface Degradation of $Li_{1−x}Ni_{0.80}Co_{0.15}Al_{0.05}O_2$ Cathodes: Correlating Charge Transfer Impedance with Surface Phase Transformations. *Appl. Phys. Lett.* **2016**, *108*, 263902.

(21) Xu, B.; Fell, C. R.; Chi, M.; Meng, Y. S. Identifying Surface Structural Changes in Layered Li-Excess Nickel Manganese Oxides in High Voltage Lithium Ion Batteries: A Joint Experimental and Theoretical Study. *Energy Environ. Sci.* **2011**, *4*, 2223−2233.

(22) Lin, F.; Markus, I. M.; Nordlund, D.; Weng, T.-C.; Asta, M. D.; Xin, H. L.; Doeff, M. M. Surface Reconstruction and Chemical

Evolution of Stoichiometric Layered Cathode Materials for Lithium-Ion Batteries. *Nat. Commun.* **2014**, *5*, 3529.

(23) Mohanty, D.; Dahlberg, K.; King, D. M.; David, L. A.; Sefat, A. S.; Wood, D. L.; Daniel, C.; Dhar, S.; Mahajan, V.; Lee, M.; Albano, F. Modification of Ni-Rich FCG NMC and NCA Cathodes by Atomic Layer Deposition: Preventing Surface Phase Transitions for High-Voltage Lithium-Ion Batteries. *Sci. Rep.* **2016**, *6*, 26532.

(24) Urban, A.; Lee, J.; Ceder, G. Electrodes: The Configurational Space of Rocksalt-Type Oxides for High-Capacity Lithium Battery Electrodes. *Adv. Energy Mater.* **2014**, *4*, 1400478.

(25) Abdellahi, A.; Urban, A.; Dacek, S.; Ceder, G. Understanding the Effect of Cation Disorder on the Voltage Profile of Lithium Transition-Metal Oxides. *Chem. Mater.* **2016**, *28*, 5373−5383.

(26) Sanchez, J.; Ducastelle, F.; Gratias, D. Generalized Cluster Description of Multicomponent Systems. *Phys. A* **1984**, *128*, 334−350.

(27) Fontaine, D. D. Cluster Approach to Order-Disorder Transformations in Alloys. *Solid State Phys.* **1994**, *47*, 33−176.

(28) Li, W.; Reimers, J. N.; Dahn, J. R. Lattice-Gas-Model Approach to Understanding the Structures of Lithium Transition-Metal Oxides $LiMO_2$. *Phys. Rev. B: Condens. Matter Mater. Phys.* **1994**, *49*, 826−831.

(29) *CASM*, v0.1.0. https://github.com/prisms-center/CASMcode.

(30) Puchala, B.; Van der Ven, A. Thermodynamics of the Zr-O System from First-Principles Calculations. *Phys. Rev. B: Condens. Matter Mater. Phys.* **2013**, *88*, 094108.

(31) Thomas, J. C.; Van der Ven, A. Finite-Temperature Properties of Strongly Anharmonic and Mechanically Unstable Crystal Phases from First-Principles. *Phys. Rev. B: Condens. Matter Mater. Phys.* **2013**, *88*, 214111.

(32) Van der Ven, A.; Thomas, J.; Xu, Q.; Bhattacharya, J. Linking the Electronic Structure of Solids to Their Thermodynamic and Kinetic Properties. *Mathem. Comput. Simul.* **2010**, *80*, 1393−1410.

(33) Ceder, G. A Derivation of the Ising Model for the Computation of Phase Diagrams. *Comput. Mater. Sci.* **1993**, *1*, 144−150.

(34) Ceder, G. The First-Principles Calculation of Phase Stability and Thermodynamic Properties. *Curr. Opin. Solid State Mater. Sci.* **1998**, *3*, 533−537.

(35) Ceder, G.; Tepesch, P. D.; Kohan, A. F.; Van der Ven, A. A Model to Predict Ionic Disorder and Phase Diagrams: Application to CaO-MgO, Gd_2O_3-ZrO_2, and to Sodium β-alumina. *J. Electroceram.* **1997**, *1*, 15−26.

(36) Van der Ven, A.; Aydinol, M. K.; Ceder, G. First-Principles Evidence for Stage Ordering in Li_xCoO_2. *J. Electrochem. Soc.* **1998**, *145*, 2149−2155.

(37) Ceder, G.; Van der Ven, A. Phase Diagrams of Lithium Transition Metal Oxides: Investigations From First Principles. *Electrochim. Acta* **1999**, *45*, 131−150.

(38) Nelson, L. J.; Hart, G. L. W.; Zhou, F.; Ozoliņš, V. Compressive Sensing as a Paradigm for Building Physics Models. *Phys. Rev. B: Condens. Matter Mater. Phys.* **2013**, *87*, 035125.

(39) Huang, W.; Kitchaev, D. A.; Dacek, S. T.; Rong, Z.; Urban, A.; Cao, S.; Luo, C.; Ceder, G. Finding and Proving the Exact Ground State of a Generalized Ising Model by Convex Optimization and MAX-SAT. *Phys. Rev. B: Condens. Matter Mater. Phys.* **2016**, *94*, 134424.

(40) Luo, C.; Cai, S.; Wu, W.; Jie, Z.; Su, K. CCLS: An Efficient Local Search Algorithm for Weighted Maximum Satisfiability. *IEEE Trans. Comput.* **2015**, *64*, 1830−1843.

(41) Kohn, W.; Sham, L. J. Self-Consistent Equations Including Exchange and Correlation Effects. *Phys. Rev.* **1965**, *140*, A1133−A1138.

(42) Kresse, G.; Furthmüller, J. Efficient Iterative Schemes for *Ab Initio* Total-Energy Calculations using a Plane-Wave Basis Set. *Phys. Rev. B: Condens. Matter Mater. Phys.* **1996**, *54*, 11169−11186.

(43) Perdew, J. P.; Burke, K.; Ernzerhof, M. Generalized Gradient Approximation Made Simple. *Phys. Rev. Lett.* **1996**, *77*, 3865−3868.

(44) Kresse, G.; Joubert, D. From Ultrasoft Pseudopotentials to the Projector Augmented-Wave Method. *Phys. Rev. B: Condens. Matter Mater. Phys.* **1999**, *59*, 1758−1775.

(45) Dudarev, S. L.; Botton, G. A.; Savrasov, S. Y.; Humphreys, C. J.; Sutton, A. P. Electron-Energy-Loss Spectra and the Structural Stability of Nickel Oxide: An LSDA+U Study. *Phys. Rev. B: Condens. Matter Mater. Phys.* **1998**, *57*, 1505−1509.

(46) Jain, A.; Hautier, G.; Moore, C. J.; Ong, S. P.; Fischer, C. C.; Mueller, T.; Persson, K. A.; Ceder, G. A High-Throughput Infrastructure for Density Functional Theory Calculations. *Comput. Mater. Sci.* **2011**, *50*, 2295−2310.

(47) Heyd, J.; Scuseria, G. E.; Ernzerhof, M. Hybrid Functionals Based on a Screened Coulomb Potential. *J. Chem. Phys.* **2003**, *118*, 8207−8215.

(48) Heyd, J.; Scuseria, G. E. Efficient Hybrid Density Functional Calculations in Solids: Assessment of the Heyd-Scuseria-Ernzerhof Screened Coulomb Hybrid Functional. *J. Chem. Phys.* **2004**, *121*, 1187−1192.

(49) Heyd, J.; Peralta, J. E.; Scuseria, G. E.; Martin, R. L. Energy Band Gaps and Lattice Parameters Evaluated with the Heyd-Scuseria-Ernzerhof Screened Hybrid Functional. *J. Chem. Phys.* **2005**, *123*, 174101.

(50) Wu, E. J.; Tepesch, P. D.; Ceder, G. Size and Charge Effects on the Structural Stability of $LiMO_2$ (M = transition metal) Compounds. *Philos. Mag. B* **1998**, *77*, 1039−1047.

(51) Chung, J.-H.; Proffen, T.; Shamoto, S.; Ghorayeb, A. M.; Croguennec, L.; Tian, W.; Sales, B. C.; Jin, R.; Mandrus, D.; Egami, T. Local Structure of $LiNiO_2$ Studied by Neutron Diffraction. *Phys. Rev. B: Condens. Matter Mater. Phys.* **2005**, *71*, 064410.

(52) Chen, H.; Freeman, C. L.; Harding, J. H. Charge Disproportionation and Jahn-Teller Distortion in $LiNiO_2$ and $NaNiO_2$: A Density Functional Theory Study. *Phys. Rev. B: Condens. Matter Mater. Phys.* **2011**, *84*, 085108.

(53) Chen, Z.; Zou, H.; Zhu, X.; Zou, J.; Cao, J. First-Principle Investigation of Jahn-Teller Distortion and Topological Analysis of Chemical Bonds in $LiNiO_2$. *J. Solid State Chem.* **2011**, *184*, 1784−1790.

(54) Rougier, A.; Delmas, C.; Chadwick, A. Non-Cooperative Jahn-Teller Effect in $LiNiO_2$: An {EXAFS} Study. *Solid State Commun.* **1995**, *94*, 123−127.

(55) Pouillerie, C.; Suard, E.; Delmas, C. Structural Characterization of $Li_{1-z-x}Ni_{1+z}O_2$ by Neutron Diffraction. *J. Solid State Chem.* **2001**, *158*, 187−197.

(56) Dyer, L. D.; Borie, B. S.; Smith, G. P. Alkali Metal-Nickel Oxides of the Type $MNiO_2$. *J. Am. Chem. Soc.* **1954**, *76*, 1499−1503.

(57) Goodenough, J.; Wickham, D.; Croft, W. Some Magnetic and Crystallographic Properties of the System Li+xNi++1−2xni+++xO. *J. Phys. Chem. Solids* **1958**, *5*, 107−116.

(58) Goodenough, J. B.; Wickham, D. G.; Croft, W. J. Some Ferrimagnetic Properties of the System $Li_xNi_{1-x}O$. *J. Appl. Phys.* **1958**, *29*, 382−383.

(59) Barton, P. T.; Premchand, Y. D.; Chater, P. A.; Seshadri, R.; Rosseinsky, M. J. Chemical Inhomogeneity, Short-Range Order, and Magnetism in the $LiNiO_2$-NiO Solid Solution. *Chem. - Eur. J.* **2013**, *19*, 14521−14531.

(60) Li, W.; Reimers, J. N.; Dahn, J. R. Crystal Structure of $Li_xNi_{2-x}O_2$ and a Lattice-Gas Model for the Order-Disorder Transition. *Phys. Rev. B: Condens. Matter Mater. Phys.* **1992**, *46*, 3236−3246.

(61) Borgers, P.; Enz, U. Metamagnetism of $NaNiO_2$. *Solid State Commun.* **1966**, *4*, 153−157.

(62) Ohzuku, T.; Ueda, A.; Nagayama, M. Electrochemistry and Structural Chemistry of $LiNiO_2$ (R $\bar{3}$m) for 4 V Secondary Lithium Cells. *J. Electrochem. Soc.* **1993**, *140*, 1862−1870.

(63) Seguin, L.; Amatucci, G.; Anne, M.; Chabre, Y.; Strobel, P.; Tarascon, J.; Vaughan, G. Structural Study of NiO_2 and CoO_2 as End Members of the Lithiated Compounds by In Situ High Resolution X-Ray Powder Diffraction. *J. Power Sources* **1999**, *81−82*, 604−606.

(64) Croguennec, L.; Pouillerie, C.; Delmas, C. NiO_2 Obtained by Electrochemical Lithium Deintercalation from Lithium Nickelate: Structural Modifications. *J. Electrochem. Soc.* **2000**, *147*, 1314−1321.

(65) Arroyo y de Dompablo, M. E.; Van der Ven, A.; Ceder, G. First-Principles Calculations of Lithium Ordering and Phase Stability on Li_xNiO_2. *Phys. Rev. B: Condens. Matter Mater. Phys.* **2002**, *66*, 064112.

(66) Reed, J.; Ceder, G. Role of Electronic Structure in the Susceptibility of Metastable Transition-Metal Oxide Structures to Transformation. *Chem. Rev.* **2004**, *104*, 4513−4534.

(67) Wang, L.; Maxisch, T.; Ceder, G. A First-Principles Approach to Studying the Thermal Stability of Oxide Cathode Materials. *Chem. Mater.* **2007**, *19*, 543−552.

(68) Reimers, J. N.; Fuller, E. W.; Rossen, E.; Dahn, J. R. Synthesis and Electrochemical Studies of $LiMnO_2$ Prepared at Low Temperatures. *J. Electrochem. Soc.* **1993**, *140*, 3396−3401.

(69) Gummow, R.; Liles, D.; Thackeray, M. Lithium Extraction from Orthorhombic Lithium Manganese Oxide and the Phase Transformation to Spinel. *Mater. Res. Bull.* **1993**, *28*, 1249−1256.

(70) Gummow, R. J.; Thackeray, M. M. An Investigation of Spinel-Related and Orthorhombic $LiMnO_2$ Cathodes for Rechargeable Lithium Batteries. *J. Electrochem. Soc.* **1994**, *141*, 1178−1182.

(71) Kötschau, I. M.; Dahn, J. R. In Situ X-Ray Study of $LiMnO_2$. *J. Electrochem. Soc.* **1998**, *145*, 2672−2677.

(72) Jang, Y.; Huang, B.; Wang, H.; Sadoway, D. R.; Chiang, Y. Electrochemical Cycling-Induced Spinel Formation in High-Charge-Capacity Orthorhombic $LiMnO_2$. *J. Electrochem. Soc.* **1999**, *146*, 3217−3223.

(73) Delmas, C.; Pérès, J.; Rougier, A.; Demourgues, A.; Weill, F.; Chadwick, A.; Broussely, M.; Perton, F.; Biensan, P.; Willmann, P. On the Behavior of the Li_xNiO_2 System: An Electrochemical and Structural Overview. *J. Power Sources* **1997**, *68*, 120−125.

(74) Li, W.; Reimers, J.; Dahn, J. In Situ X-Ray Diffraction and Electrochemical Studies of $Li_{1−x}NiO_2$. *Solid State Ionics* **1993**, *67*, 123−130.

(75) Arai, H.; Okada, S.; Ohtsuka, H.; Ichimura, M.; Yamaki, J. Characterization and Cathode Performance of $Li_{1−x}Ni_{1+x}O_2$ Prepared with the Excess Lithium Method. *Solid State Ionics* **1995**, *80*, 261−269.

(76) Delmas, C.; Ménétrier, M.; Croguennec, L.; Levasseur, S.; Pérès, J.; Pouillerie, C.; Prado, G.; Fournès, L.; Weill, F. Lithium Batteries: A New Tool in Solid State Chemistry. *Int. J. Inorg. Mater.* **1999**, *1*, 11−19.